

COMPARATIVE STUDY OF SEMICLASSICAL APPROACHES TO QUANTUM DYNAMICS

G. SCHUBERT

*Institut für Physik, Ernst-Moritz-Arndt Universität Greifswald
17487 Greifswald, Germany
schubert@physik.uni-greifswald.de*

V.S. FILINOV

*Joint Institute for High Temperatures, Russian Academy of Sciences
Moscow 127412, Russia*

K. MATYASH, R. SCHNEIDER

*Max-Planck-Institut für Plasmaphysik
17491 Greifswald, Germany*

H. FEHSKE

*Institut für Physik, Ernst-Moritz-Arndt Universität Greifswald
17487 Greifswald, Germany*

Quantum states can be described equivalently by density matrices, Wigner functions or quantum tomograms. We analyze the accuracy and performance of three related semiclassical approaches to quantum dynamics, in particular with respect to their numerical implementation. As test cases, we consider the time evolution of Gaussian wave packets in different one-dimensional geometries, whereby tunneling, resonance and anharmonicity effects are taken into account. The results and methods are benchmarked against an exact quantum mechanical treatment of the system, which is based on a highly efficient Chebyshev expansion technique of the time evolution operator.

Keywords: Time evolution of quantum systems; Wigner function; quantum tomography; semiclassical approximation; Chebyshev expansion

PACS Nos.: 03.65.Sq, 03.65.Wj

Introduction

Quantum statistical physics, such as condensed matter or plasma physics, but also quantum chemistry, heavily depends on effective numerical methods for solving

Electronic version of an article published as DOI:10.1142/S0129183109014278
International Journal of Modern Physics C, Vol. 20, No. 8 (2009) pp. 1155 - 1186,
© World Scientific Publishing Company, <http://www.worldscinet.com/ijmpc/ijmpc.shtml>

complex few- and many particle problems. Implementing suitable theoretical concepts for their description on modern (super-) computer architectures, nowadays computational physics constitutes, besides experiment and theory, the third column of contemporary physics¹. Numerical techniques become especially important for strongly correlated systems where analytical approaches largely fail. This may be due to the absence of small (coupling) parameters or, more general, because the relevant energy scales are not well separated, both preventing the application of standard perturbative schemes. Another challenging problem, that calls for numerical approaches, concerns the description of microscopic and nanoscopic systems, and of particles in finite quantum structures (restricted geometries), where the level quantization might become as important as particle correlations.

A first idea for the numerical study of this kind of quantum systems might be a brute force exact diagonalization of the underlying (model) Hamiltonian. Considering the exponential growth of the Hilbert space with the number of particles, such a description of quantum many-particle systems is (and will be in the future) out of reach. The situation becomes even more difficult if bosonic degrees of freedom (e.g. phonons in a solid) come into play, resulting in an infinite dimensional Hilbert space even for finite systems. One way to circumvent this problem is to restrict the many-particle Hilbert space to the physically most important subset. Along this line, e.g., density matrix renormalization group schemes have been developed^{2,3}. Semiclassical descriptions offer another possibility to overcome these limitations. A variety of semiclassical methods has been proposed during the last decades, especially to describe the dynamics of quantum systems^{4,5,6,7,8,9}. These methods are appealing, in some sense, as their close relation to concepts familiar from classical physics facilitates an intuitive interpretation of the results. Also in view of bridging the gap between quantum many-particle and classical continuum theories they seem promising for describing systems in the thermodynamic limit. Therefore we will focus on semiclassical approaches to quantum dynamics in the following, of which we will discuss three carefully selected ones in more detail.

The majority of the traditional semiclassical methods is based on a real time path integral formulation of quantum mechanics^{10,11}. Expressing the time evolution of the complex wave function in terms of action integrals, the Feynman path integral is generally evaluated within the stationary-phase approximation. Then the occurring integrals can sometimes be performed analytically, otherwise numerically using direct integration or Monte Carlo (MC) techniques¹². Integrating an oscillatory, complex valued integrand, the dynamical sign problem, however, spoils to some extent the efficiency of the MC integration. Despite the exponential decay of the integrand outside a vicinity of the classical trajectories the numerics is still challenging. In the sum of many contributions with different complex phases most of them may cancel out and the result may become exponentially small.

Equivalently, a quantum system can be described in terms of real valued quantum phase space distribution functions¹³, e.g., the Wigner function¹⁴. This overcomes the problem of handling a complex valued wave function but, because of

possible negative values of the Wigner function and the Heisenberg uncertainty relation, the Wigner function cannot be interpreted as a joint probability. Instead, it should be considered as a convenient mathematical tool for the description of quantum systems. In the numerical work, the dynamical sign problem is alleviated for the Wigner function but still present^{15,16,17}.

In order to overcome the heavily debated dynamical sign problem, some years ago the description of quantum states in terms of a positive function, the so called quantum tomogram, has been proposed^{18,19}. The strict positivity of the tomogram seems promising in view of an effective MC sampling of the trajectories. In the framework of the tomographic representation a description of quantum dynamics by diffusive Markov processes was suggested in²⁰. Recently, the applicability of the tomographic approach to one- and two-particle systems has been demonstrated^{21,22}. However, to the best of our knowledge, most of those studies are based on harmonic potentials but validations for arbitrarily shaped potentials are still missing.

Motivated by this situation, it is the aim of the present work, to outline and compare the various methods quoted above with respect to their accuracy and computational performance. The selected semiclassical methods were chosen to represent algorithms based on different descriptions of quantum states: the wave function, the Wigner function and the quantum tomogram. Instead of investigating complex physical systems in which a multitude of effects compete, we benchmark the methods on the basis of relatively simple systems, concentrating onto a single aspect in each case. We will focus on the dynamics of a wave packet in distinct model geometries which account for basic aspects of quantum mechanics: tunneling, confinement and nonlinearity (anharmonicity). Calibrating the different approaches by studying simple toy models is necessary in order to detect their limitations and prospects, before applying them to the more complicated problems of current interest, e.g., to classical chaotic systems, quantum localisation, dynamic tunneling or entanglement. The obtained semiclassical results will be compared with an exact solution for the time evolution of the quantum system. Thereby, the exact solution is calculated using a highly efficient expansion of the time evolution operation in a series of Chebyshev polynomials.

1. Computational schemes

1.1. Chebyshev expansion of the time evolution operator

As a reference for the approximate results we will present in the next sections, the Chebyshev expansion of the time evolution operator constitutes a very efficient technique which fully includes all quantum effects. Governed by the time dependent Schrödinger equation, the dynamics of a quantum state $|\psi(t_0)\rangle$ in a time independent external potential may be expressed in terms of the time evolution operator $U(t, t_0) = U(\Delta t) = e^{-iH(t-t_0)/\hbar}$ with $\Delta t = t - t_0$. Expanding $U(\Delta t)$ into a series of first kind Chebyshev polynomials of order k , $T_k(x) = \cos(k \arccos(x))$,^{23,24,25}, we

obtain

$$U(\Delta t) = e^{-ib\Delta t/\hbar} \left[c_0(a\Delta t/\hbar) + 2 \sum_{k=1}^M c_k(a\Delta t/\hbar) T_k(\tilde{H}) \right]. \quad (1)$$

Prior to the expansion, the Hamiltonian has to be shifted and rescaled such that the spectrum of $\tilde{H} = (H - b)/a$ is within the definition interval of the Chebyshev polynomials, $[-1, 1]$. The parameters a and b are calculated from the extreme eigenvalues of H as $b = \frac{1}{2}(E_{\max} + E_{\min})$ and $a = \frac{1}{2}(E_{\max} - E_{\min} + \epsilon)$. Here, we introduced $\epsilon = \alpha(E_{\max} - E_{\min})$ to ensure the rescaled spectrum $|\tilde{E}| \leq 1/(1 + \alpha)$ to be well inside $[-1, 1]$. In practice, we use $\alpha = 0.01$. Note, that the Chebyshev expansion also applies to systems with unbounded spectra. In those cases we truncate the infinite Hilbert space to a finite dimension by restricting the model on a discrete space grid or using an energy cutoff. By this, we ensure possibly large but finite extreme eigenvalues.

In (1), the expansion coefficients $c_k(a\Delta t/\hbar)$ are given by

$$c_k(a\Delta t/\hbar) = \int_{-1}^1 \frac{T_k(x) e^{-ix a \Delta t/\hbar}}{\pi \sqrt{1-x^2}} dx = (-i)^k J_k(a\Delta t/\hbar), \quad (2)$$

where J_k denotes the k -th order Bessel function of the first kind.

To calculate the evolution of a state $|\psi(t_0)\rangle$ from one time grid point to the next one, $|\psi(t)\rangle = U(\Delta t)|\psi(t_0)\rangle$, we have to accumulate the c_k -weighted vectors $|v_k\rangle = T_k(\tilde{H})|\psi(t_0)\rangle$. Since the coefficients $c_k(a\Delta t/\hbar)$ depend on the time step but not on time explicitly, we need to calculate them only once. The vectors $|v_k\rangle$ can then be calculated iteratively using the recurrence relation of the Chebyshev polynomials

$$|v_{k+1}\rangle = 2\tilde{H}|v_k\rangle - |v_{k-1}\rangle, \quad (3)$$

where $|v_1\rangle = \tilde{H}|v_0\rangle$ and $|v_0\rangle = |\psi(t_0)\rangle$.

In the numerics, we use a discrete coordinate space basis $|q_i\rangle$, $i = 1, \dots, N$ with $\langle q|q_i\rangle = \delta(q - q_i)$, representing an equally spaced grid of N points. The wave function at position q_i is given by the i -th entry of the corresponding (complex) vector, $\psi(q_i, t_0) = \langle q_i|\psi(t_0)\rangle$. Aiming at the description of a spatially unbounded system, we choose the extension of our space grid such that $\psi(q_1, t) = \psi(q_N, t) \equiv 0$ throughout the whole simulation. In this way, no artificial reflections at the boundaries of the simulation volume arise and the results are independent of the actual size of the simulation volume. Overall, evolving the wave function from one time step to the next requires M matrix vector multiplications (MVM) of a given complex vector with the (sparse) Hamiltonian of dimension N as well as the summation of the resulting vectors after appropriate scaling:

$$|\psi(t)\rangle = e^{-ib\Delta t/\hbar} \left[J_0(a\Delta t/\hbar) + 2 \sum_{k=1}^M (-i)^k J_k(a\Delta t/\hbar) T_k(\tilde{H}) \right] |\psi(t_0)\rangle. \quad (4)$$

Note that the Chebyshev expansion may also be applied to systems with time dependent Hamiltonians. However, there the time variation $H(t)$ determines the

maximum Δt by which the system may be propagated in one time step. For time independent H , in principle, arbitrary large time steps are possible at the expense of increasing M .

1.2. Linearized semiclassical propagator method

Aiming at the description of a many-particle system, the numerical effort for a full quantum calculation increases drastically. If the system is described in terms of (correctly symmetrized) product states, the main numerical problem is the exponential growth of the Hilbert space dimension with the number of particles. For some systems, the full correlations encoded in those states are of minor importance as particular aspects of interest may be described on a lower level of complexity. Therefore, much interest has been devoted to finding a suitable semiclassical approximation for the time evolution operator. Based on a path integral description of quantum mechanics^{10,11}, the Suzuki-Trotter decomposition^{26,27} of $U(t-t_0)$ opens the road toward a class of semiclassical approximations. Instead of directly propagating the quantum state as a whole using $U(t-t_0)$, we consider the propagation of several individual paths from $q_0(t_0)$ to $q(t)$ (virtual particle trajectories). The corresponding propagator is given by

$$\Pi(q, t; q_0, t_0) \sim \sum_{\substack{\text{v. paths} \\ q_0 \rightsquigarrow q}} C \exp(iS(q, t; q_0, t_0)/\hbar) , \quad (5)$$

with some normalization factor C and the action

$$S(q, t; q_0, t_0) = \int_{t_0}^t dt' p(t') \dot{q}(t') - H[p(t'), q(t')] , \quad (6)$$

evaluated along each virtual path. $H(p, q)$ is the classical Hamilton function of the system. The only restriction for the virtual paths are fixed starting and end points, $q_0(t_0)$ and $q(t)$, apart from which they are completely arbitrary. Specifically, they do not follow the Hamilton equations of motion, which only hold for a subset of them, namely the classical paths (left panel of Fig. 1).

In a numerical implementation (middle panel of Fig. 1), the quantum state is represented on a discrete coordinate grid \tilde{q}_i for any time grid point, while the coordinates of the virtual trajectories are treated as continuous variables. Reconstructing the quantum state at time t involves the integration over the propagators between all possible combinations of q_0 and q . While we choose the q_0 from the set of discrete grid points, the end points q may also be off the grid. For the deposition²⁸ of a trajectory to the \tilde{q}_i grid, a suitable shape function $\Lambda(\tilde{q}_i, q)$, e.g., a Gaussian or simply a delta peak at the nearest grid point, is necessary,

$$\psi(\tilde{q}_i, t) = \int dq_0 \int dq \Lambda(\tilde{q}_i, q) \Pi(q, t; q_0, t_0) \psi(q_0, t_0) . \quad (7)$$

As the contributions to $\psi(\tilde{q}_i, t)$ from the different paths are complex valued, their superposition includes interference effects in the reconstructed quantum state. The

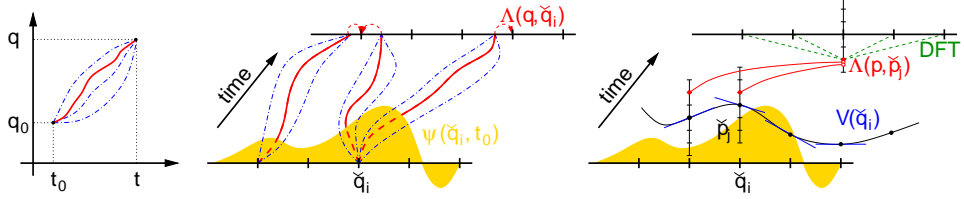


Fig. 1. Left panel: Virtual (blue, dashed-dotted lines) and classical (red, solid line) paths connecting $q_0(t_0)$ and $q(t)$. For the classical path the action along the trajectory is extremal. Middle panel: Visualization of the deposition scheme (7). At each coordinate grid point \tilde{q}_i the initial wave function $\psi(\tilde{q}_i, t_0)$ determines the sampling weight for all trajectories starting from \tilde{q}_i . The path propagation follows the classical equations of motion and the virtual (non-extremal) paths are taken into account perturbatively. As the end points of the paths $q(t)$ need not match the grid, they are deposited there using the shape function $\Lambda(q, \tilde{q}_i)$. Right panel: Wave function propagation as implemented in this work. Around each grid point the potential is approximated to first order. The propagator for a constant force field is known analytically. Starting from all possible pairs of initial conditions (q_i, p_j) , $i, j = 1, \dots, N$, the trajectories are deposited in momentum space, matched to the momentum grid by $\Lambda(p, \tilde{p}_j)$. The reconstruction of the wave function in coordinate space is done by inverse discrete Fourier transform.

major difference between existing semiclassical propagator methods concerns the numerical implementation of (7). The standard line of argumentation in the literature is that the main contributions to (5) are those for which S is extremal – these are just the classically realized trajectories – and the paths in their vicinity. This requirement is deduced from stationary phase integration. Then, the action is expanded to second order around the extremal trajectories giving the well known WKB^{29,30,31} result^{32,33}

$$\Pi^{\text{WKB}}(q, t; q_0, t_0) = \sum_{\substack{\text{c.paths} \\ q_0 \leadsto q}} \sqrt{\frac{i}{2\pi\hbar} \frac{\partial^2 S_c}{\partial q_0 \partial q}} \exp\left(\frac{i}{\hbar} S_c(q, t; q_0, t_0)\right), \quad (8)$$

where $S_c(q, t; q_0, t_0)$ is the action along the extremal trajectories from $q_0(t_0)$ to $q(t)$ and the phase of \sqrt{i} is fixed to $\pi/4$. The sum accounts for the fact that specifying q_0 and q does not uniquely determine a classical trajectory. In addition to the phase factor from the classical action, the phase of the propagator is determined by the sign of $\partial^2 S_c / (\partial q_0 \partial q)$. Using $p_0 = -\partial S_c / \partial q_0$, the Morse theory^{34,35} allows for separating the determinant of the monodromy matrix $\partial q / \partial p_0$ from its sign. Relating the number of focal points (at which $\partial q / \partial p_0$ vanishes) along a trajectory to the number of negative eigenvalues of $\partial^2 S_c / (\partial q \partial q_0)$, the whole phase information can be encoded in the Morse index ν . For each focal point, ν is increased by one, and the square root is taken from the absolute value of $\partial q / \partial p_0$. Then we obtain the Van Vleck Gutzwiller propagator^{36,37}

$$\Pi^{\text{VG}}(q, t; q_0, t_0) = \frac{1}{\sqrt{2\pi i \hbar}} \sum_{\substack{\text{c.paths} \\ q_0 \leadsto q}} \left| \frac{\partial q}{\partial p_0} \right|^{-1/2} e^{i S_c(q, t; q_0, t_0) / \hbar} e^{-i \pi \nu / 2}. \quad (9)$$

In view of a numerical evaluation, this formulation has several shortcomings. First,

the so called root search problem consists in finding all initial momenta p_0 for which trajectories starting in q_0 end up in q . For complex systems, this boundary value problem is much more demanding than the solution of an initial value problem. Second, at the focal points the expression (9) diverges and the expansion of S has to be taken to higher order. At those points it is particularly difficult to keep track of the correct branch of the square root of $\partial q/\partial p_0$ and thus determining the Morse index. Both problems are circumvented in contemporary applications of the semiclassical propagator by expressing (9) in an initial value representation (SCIVR) ^{4,5,38}. Inserting (9) into (7), this is achieved by a change of variables,

$$\int dq_0 \int dq \sum_{\substack{\text{c.paths} \\ q_0 \rightsquigarrow q}} \rightarrow \int dq_0 \int dp_0 \left| \frac{\partial q}{\partial p_0} \right|, \quad (10)$$

circumventing the root search, and the monodromy matrix appears in the numerator,

$$\begin{aligned} \psi^{\text{SCIVR}}(\check{q}_i, t) = & \frac{1}{\sqrt{2\pi i \hbar}} \int dq_0 \int dp_0 \Lambda(\check{q}_i, q(q_0, p_0)) \left| \frac{\partial q(q_0, p_0)}{\partial p_0} \right|^{1/2} \\ & \times e^{iS(t; q_0, p_0, t_0)/\hbar} e^{-i\pi\nu/2} \psi(q_0, t_0). \end{aligned} \quad (11)$$

Here, the final coordinate $q(q_0, p_0)$ is a deterministic function of the initial values q_0, p_0 . Instead of using a coordinate space basis, similar methods have been formulated in momentum or coherent state representation ^{38,39,40}, leading to the Herman-Kluk propagator ^{41,42}. For all these methods the problem of the oscillatory integrand still persists. To improve the convergence properties of the MC integrals, various integral filtering techniques have been proposed in the literature ^{12,40,43,44}. Thereby, the basic idea is to filter out the high frequency oscillations of the integrand which contribute only little to the integral but are the main obstacle for an efficient MC evaluation.

In this work, we follow a recently proposed ^{45,46}, slightly different route (cf. right panel of Fig. 1). Discretizing the potential on the coordinate grid \check{q}_i , we locally approximate the potential to first order and use this approximation for $\check{q}_i - \Delta\check{q}/2 < q < \check{q}_i + \Delta\check{q}/2$. A justified question then is, to which extent the concatenated potential will be able to fully describe quantum effects and reproduce the results for the original continuous potential. The propagator for a trajectory in a linear potential is known analytically ⁴⁷,

$$\begin{aligned} \Pi^{\text{lin}}(q, t; q_0, t_0) = & \sqrt{\frac{m}{2\pi i \hbar (t - t_0)}} \\ & \times \exp \left[\frac{i}{\hbar} \left(\frac{m(q - q_0)^2}{2(t - t_0)} - \frac{s}{2}(q + q_0)(t - t_0) - \frac{s^2(t - t_0)^3}{24m} \right) \right], \end{aligned} \quad (12)$$

where s is the slope of the potential. In contrast to the WKB formulation, here tracking the sign of the monodromy matrix is not necessary, but the maximum

possible time step is severely reduced. This limit is set by the validity of the local potential approximation, i.e., by the potential variation and grid spacing. The time step has to be chosen such that even the fastest particles stay within their initial grid cells intermediately. An advantage of the constant force field approximation is the bijection between final positions and initial momenta which allows for a straight forward formulation of the algorithm in terms of an initial value representation. The range of initial momenta, which are required by Fourier completeness is given by the coordinate grid spacing as $|p_0| \leq \pi\hbar/\Delta\check{q}$. A final trick consists in depositing the contributions from all virtual particles not directly to the coordinate grid. Instead, they are gathered in momentum space and the reconstructed wave function in coordinate space is obtained using inverse discrete Fourier transform,

$$\psi(\check{q}_i, t) = \sum_{j=1}^N \frac{\Delta\check{p}}{\sqrt{2\pi\hbar}} \exp\left(\frac{2\pi i\check{q}_i\check{p}_j}{\hbar N}\right) \psi(\check{p}_j, t). \quad (13)$$

This mixed representation has proven less noisy than a direct deposition in coordinate space³⁸. In analogy to (7), we use the shape function $\Lambda(\check{p}_j, p)$ for the deposition on the momentum grid

$$\psi(\check{p}_j, t) = \int dq_0 \int dp \Lambda(\check{p}_j, p) \Pi^{\text{lin}}(p, t; q_0, t_0) \psi(q_0, t_0), \quad (14)$$

where $\Pi^{\text{lin}}(p, t; q_0, t_0)$ is the Fourier transform of (12),

$$\Pi^{\text{lin}}(p, t; q_0, t_0) = \frac{1}{\sqrt{2\pi\hbar}} \int dq \Pi^{\text{lin}}(q, t; q_0, t_0) e^{-ipq/\hbar}. \quad (15)$$

Instead of an explicit evaluation of the q -integral in (15), we profit from the knowledge about the trajectories,

$$q(t) = -\frac{s}{2m}(t-t_0)^2 + \frac{p_0}{m}(t-t_0) + q_0, \quad (16)$$

to change the integration variable from q to p_0 . Finally, this allows us to propagate the wave function by one time step, $\Delta t = t - t_0$, using an initial value representation,

$$\begin{aligned} \psi^{\text{lin}}(\check{q}_i, t) &= \sum_{j=1}^N \frac{\Delta\check{p}}{2\pi\hbar} \exp\left(\frac{2\pi i\check{q}_i\check{p}_j}{\hbar N}\right) \int dp \Lambda(\check{p}_j, p) \sqrt{\frac{1}{2\pi i\hbar} \frac{\Delta t}{m}} \int dq_0 \int dp_0 \psi(q_0, t_0) \\ &\times \exp\left[\frac{i}{\hbar} \left(\frac{m[q(q_0, p_0) - q_0]^2}{2\Delta t} - \frac{s\Delta t}{2} [q(q_0, p_0) + q_0] - \frac{s^2(\Delta t)^3}{24m} - pq(q_0, p_0) \right)\right], \end{aligned} \quad (17)$$

where $q(q_0, p_0)$ is given in (16).

1.3. Wigner-Moyal approach

Dating back to Wigner¹⁴, the idea of describing quantum mechanics without a complicated operator algebra, but by equations for commuting variables, has been very appealing. Then, introducing a phase space distribution function and replacing

operator expressions according to the corresponding rules of association, quantum expectation values may be calculated by simple integration over commuting variables. One of the most common¹³ distribution functions is the Wigner function,

$$W(q, p, t) = \frac{1}{2\pi} \int e^{-i\eta p} \psi^*(q - \eta\hbar/2, t) \psi(q + \eta\hbar/2, t) d\eta, \quad (18)$$

together with the corresponding Weyl rule of association⁴⁸. Within this rule of association, operator expressions ordered as $e^{i\xi\hat{q}+i\eta\hat{p}}$ are replaced by their scalar variables, e.g., $e^{i\xi\hat{q}+i\eta\hat{p}} \leftrightarrow e^{i\xi q+i\eta p}$, with $\xi, \eta \in \mathbb{C}$. Starting from the von Neumann equation for the time evolution of the density matrix, we determine the evolution equation for the Wigner function^{16,17,49} as

$$\frac{\partial W}{\partial t} + \frac{p}{m} \frac{\partial W}{\partial q} + F(q) \frac{\partial W}{\partial p} = \int_{-\infty}^{\infty} ds W(q, p-s, t) \omega(s, q), \quad (19)$$

where $F(q) = -\frac{dV(q)}{dq}$ is the classical force, and

$$\omega(s, q) = \frac{2}{\pi\hbar^2} \int dq' V(q-q') \sin\left(\frac{2sq'}{\hbar}\right) + F(q) \frac{d\delta(s)}{ds}. \quad (20)$$

In the classical limit, the right hand side of (19) vanishes, leaving us with the Liouville equation for the phase space density. Then the dynamics can be expressed in terms of the classical propagator

$$\Pi^W(q, p, t; q_0, p_0, t_0) = \delta[q - \bar{q}(t; p_0, q_0, t_0)] \delta[p - \bar{p}(t; p_0, q_0, t_0)]. \quad (21)$$

Here \bar{p} and \bar{q} are the momentum and coordinate of a trajectory which evolves according to the Hamilton equations of motion subject to the initial conditions $\bar{p}(t_0) = p_0$ and $\bar{q}(t_0) = q_0$. Using Π^W , we may rewrite (19) in form of an integral equation^{15,16,17},

$$\begin{aligned} W(q, p, t) &= \int dp_0 dq_0 \Pi^W(q, p, t; q_0, p_0, t_0) W_0(q_0, p_0, t_0) \\ &+ \int_{t_0}^t d\tau \int dp_\tau dq_\tau \Pi^W(q, p, t; q_\tau, p_\tau, \tau) \int_{-\infty}^{\infty} ds W(q_\tau, p_\tau - s, \tau) \omega(s, q_\tau), \end{aligned} \quad (22)$$

and solve it by iteration. To lowest order, we only keep the first line in (22) and neglect the second integral completely. This means, we propagate classical trajectories (\bar{q}, \bar{p}) in time, after sampling their initial conditions p_0 and q_0 from the initial Wigner function $W_0(q_0, p_0, t_0)$ at time t_0 using a MC procedure. Assembling those contributions at the next time grid point $t = t_0 + \Delta t$, we obtain the lowest order approximation $W^{(1)}(q, p, t)$.

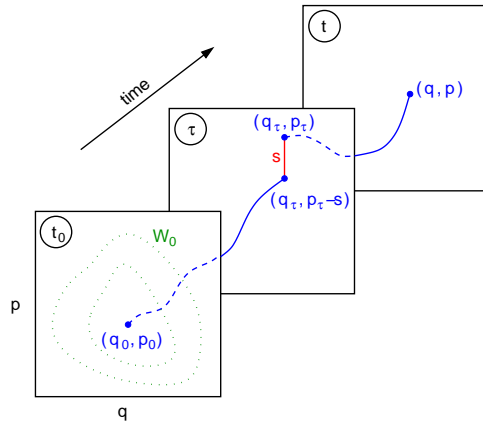


Fig. 2. Cartoon of propagating one trajectory in presence of momentum jumps. At time t_0 , the initial conditions for the trajectory (q_0, p_0) are sampled from $W_0(q_0, p_0, t_0)$ by a MC procedure. Then up to time $\tau \in [t_0, t]$ this trajectory is propagated to $(q_\tau, p_\tau - s)$ according to the classical equations of motion. There, an instantaneous change in momentum by s occurs, leaving the intermediate position q_τ fixed. From the new phase space point (q_τ, p_τ) the trajectory evolves again classically up to t , following the propagator $\Pi^W(q, p, t; q_\tau, p_\tau, \tau)$. When summing up the contributions of all trajectories, each one has to be weighted by the function $\omega(s, q_\tau)$, accounting for the momentum jump s and the potential at the intermediate position q_τ .

For the second order approximation, $W^{(2)}(q, p, t)$, we expand the Wigner function in the last integral in (22) consistently to lowest order,

$$\begin{aligned} W(q_\tau, p_\tau - s, \tau) &\approx W^{(1)}(q_\tau, p_\tau - s, \tau) \\ &= \int dp_0 dq_0 \Pi^W(q_\tau, p_\tau - s, \tau; q_0, p_0, t_0) W_0(q_0, p_0, t_0). \end{aligned} \quad (23)$$

This allows for evaluating $W^{(2)}$ also by means of trajectory methods. A sketch of the basic idea behind the second order approximation is given in Fig. 2, together with a detailed description in the caption. Including momentum jumps in the evolution of $W^{(2)}$ we take into account that continuous phase space trajectories are guaranteed only for classical or almost classical systems¹³. Depending on the momentum jump s and the potential $V(q_\tau - q')$, the weighting factor $\omega(s, q_\tau)$ may become negative. Therefore, sign changes of the Wigner function at some phase space points are included in the second order approximation, whereas they are absent in the first order approximation due to strictly positive trajectory weights.

Using the improved estimate $W^{(2)}$ in (23), the construction of higher order terms is straight forward. Conceptually, higher order terms correspond to the inclusion of several momentum jumps within one time step. As the fundamental aspects (discontinuous trajectories, possibility of negative trajectory weights) are already included in $W^{(2)}$, we restrict ourselves to the two lowest orders of the approximation. A detailed investigation of the inclusion of higher order terms is beyond the scope of this work (for details see^{15,16}).

Having $W(q, p, t)$ at hand, it is not difficult to calculate expectation values of all kinds of operators from it. For any operator expression which is ordered as $e^{i\xi\hat{q}+i\eta\hat{p}}$, we follow the Weyl rule of association and replace each operator by its corresponding scalar function. After multiplication with the Wigner function we integrate over the whole phase space and obtain the desired expectation value.

1.4. *Tomographic approach*

In view of a probabilistic interpretation of quantum mechanics, the Wigner function has the shortcoming of possible negative values, which prevents its interpretation as a probability density. Furthermore, any interpretation of a joint probability, that simultaneously determines coordinate and momentum for a quantum system, violates the Heisenberg uncertainty relation and is therefore misleading. Meaningful results for probabilities and expectation values, are integrals over the Wigner function in extended phase space regions, e.g., minimum uncertainty Gaussians, or along phase space contours. Such a contour integration is used in the tomographic representation of quantum mechanics proposed some years ago^{18,19}. The so called quantum tomogram^{21,50},

$$\tilde{w}(X, \mu, \nu, t) = \int \frac{dk dq dp}{2\pi} W(q, p, t) e^{-ik(X - \mu q - \nu p)}, \quad (24)$$

relates to the Wigner function by a class of Radon transformations⁵¹ which are characterized by μ and ν . A simple, intuitive interpretation of the quantum tomogram is shown in Fig. 3(a). The vector (μ, ν) fixes a direction, with X the distance from the origin. Then the tomogram $\tilde{w}(X, \mu, \nu)$ is just the integral over the Wigner function along a straight line perpendicular to (μ, ν) which passes through X . Choosing (μ, ν) appropriately, we may continuously change between coordinate and momentum representation. Describing a quantum system in terms of the tomogram is completely equivalent to the wave function or Wigner function representation. Its relation to the Wigner function is obvious due to its definition, and we obtain the Wigner function from the tomogram by the inverse map

$$W(q, p, t) = \int \frac{dX d\mu d\nu}{(2\pi)^2} \tilde{w}(X, \mu, \nu, t) e^{i(X - \mu q - \nu p)}. \quad (25)$$

The relation to the wave function formalism is a little more involved. We may extract the probability densities in any rotated reference frame (in particular coordinate and momentum space) from the tomogram, but not the wave function itself. The phase information inherent to the wave function is distributed over all reference frames (μ, ν) . Each fixed choice of (μ, ν) gives only a density information, e.g., the coordinate representation $|\psi(q)|^2$ is equal to $\tilde{w}(X, \mu = 1, \nu = 0)$. Keeping this aspect in mind as well as the larger required set of variables, one might ask at this point what the profit of this method shall be. Considering the dynamics of a quantum system, the strict positivity of the tomogram is its main numerical advantage. This

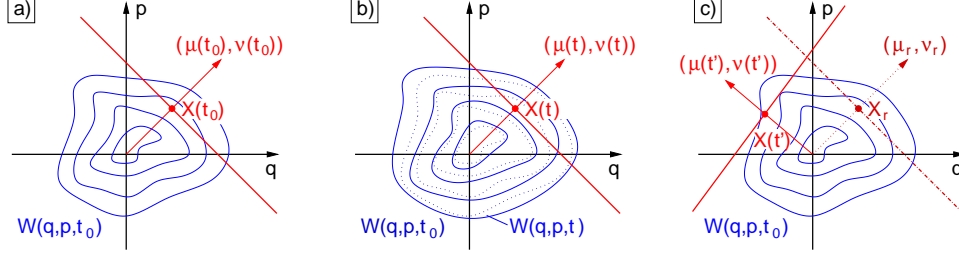


Fig. 3. Cartoon of the quantum tomogram and its time evolution. Panel (a): The tomogram $\bar{w}(X(t_0), \mu(t_0), \nu(t_0), t_0)$ is the integral over $W(q, p, t_0)$ along the thick red line. Panel (b): Extraction of the tomogram in the same reference frame at time t by evolving the Wigner function and keeping $(\mu_r, \nu_r) = [\mu(t), \nu(t)] = [\mu(t_0), \nu(t_0)]$ fixed. Panel (c): Time evolution of the tomogram by the method of characteristics. Keeping the Wigner function $W(q, p, t_0)$ fixed, $(\mu_r, \nu_r) = [\mu(t), \nu(t)]$ is propagated backward in time to $(\mu(t'), \nu(t'))$ using (29) for different local approximations. Summing all those contributions gives the tomogram at t in the desired reference frame (μ_r, ν_r) .

circumvents the dynamical sign problem encountered in the Wigner function and semiclassical propagator approaches.

The time evolution of the tomogram can be thought of in two equivalent ways. For any reference frame $(\mu(t_0), \nu(t_0))$, e.g., the coordinate representation $(1, 0)$, the tomogram can be calculated for all times by keeping (μ, ν) fixed and evolving the Wigner function in time [Fig. 3(b)]. This is exactly the interpretation we used in Sect. 1.3 to extract $|\psi(q, t)|^2$ from the Wigner function. Alternatively, we can exploit the evolution equation of the tomogram^{20,52},

$$\frac{\partial \bar{w}}{\partial t} - \frac{\mu}{m} \frac{\partial \bar{w}}{\partial \nu} - \frac{i}{\hbar} \left[V \left(-\frac{\partial}{\partial \mu} \frac{1}{\partial / \partial X} - \frac{i\hbar\nu}{2} \frac{\partial}{\partial X} \right) - V \left(-\frac{\partial}{\partial \mu} \frac{1}{\partial / \partial X} + \frac{i\hbar\nu}{2} \frac{\partial}{\partial X} \right) \right] \bar{w} = 0, \quad (26)$$

which can be derived from the von Neumann equation. In view of the definition of \bar{w} in (24), the ‘anti-derivative’ $\partial_X^{-1} \bar{w}$ just multiplies $W(q, p)$ by i/k . Therefore, the term $\partial_\mu \partial_X^{-1} \bar{w}$ is well defined. A solution of (26) for harmonic potentials $V(q) = \frac{1}{2} m \omega_0^2 (q - q_c)^2$ can be given explicitly. In analogy to the continuity equation for the tomogram,

$$\frac{d\bar{w}}{dt} = \frac{\partial \bar{w}}{\partial t} + \frac{\partial \bar{w}}{\partial X} \dot{X} + \frac{\partial \bar{w}}{\partial \mu} \dot{\mu} + \frac{\partial \bar{w}}{\partial \nu} \dot{\nu} = 0, \quad (27)$$

we collect the terms in (26) and find the correspondences

$$\dot{X} = m\omega_0^2 q_c \nu, \quad \dot{\mu} = m\omega_0^2 \nu, \quad \dot{\nu} = -\mu/m. \quad (28)$$

This set of linear differential equations defines trajectories in (X, μ, ν) space characterizing the reference frames in Fig. 3. Solving the system (28), we get the propagator

from (X_0, μ_0, ν_0, t_0) to (X, μ, ν, t) as

$$\begin{aligned} \Pi_{\omega_0, q_c}^T(X, \mu, \nu, t; X_0, \mu_0, \nu_0, t_0) &= \delta \left[\nu + \frac{\mu_0}{m\omega_0} \sin[\omega_0(t-t_0)] - \nu_0 \cos[\omega_0(t-t_0)] \right] \\ &\times \delta \left[X - X_0 - \mu_0 q_c (\cos[\omega_0(t-t_0)] - 1) - \nu_0 m \omega_0 q_c \sin[\omega_0(t-t_0)] \right] \\ &\times \delta \left[\mu - \mu_0 \cos[\omega_0(t-t_0)] + \nu_0 m \omega_0 \sin[\omega_0(t-t_0)] \right]. \end{aligned} \quad (29)$$

The uniqueness of the $(X(t), \mu(t), \nu(t))$ trajectories is due to the q -independency of the coefficients in the set of equations (28).

Evaluating (26) for arbitrary potentials (beyond the free particle or harmonic case), higher order derivatives of \tilde{w} appear. This spoils the identification with the continuity equation (27) and the application of the method of characteristics (28). A possible way out is the local expansion of the potential to second order. Then (26)-(29) are valid locally for each q with appropriate parameters $\omega_0(q)$ and $q_c(q)$ which are determined from the harmonic expansion around q . Since now several propagators (29) exist, the (X, μ, ν) trajectories are not unique anymore, and the tomogram at the new time grid point is given by

$$\begin{aligned} \tilde{w}(X, \mu, \nu, t) &= \int dX_0 \int d\mu_0 \int d\nu_0 \int dq \\ &\Pi_{\omega_0(q), q_c(q)}^T(X, \mu, \nu, t; X_0, \mu_0, \nu_0, t_0) \tilde{w}(X_0, \mu_0, \nu_0, t_0). \end{aligned} \quad (30)$$

Usually, we are not interested in the full $\tilde{w}(X, \mu, \nu, t)$ but only in a particular reference frame (μ_r, ν_r) , e.g., the coordinate representation. Having the method of characteristics in mind, we search for those trajectories $(X(t_0), \mu(t_0), \nu(t_0))$ that give contributions to $(X(t), \mu(t), \nu(t)) = (X_r, \mu_r, \nu_r)$. To this end, we start from the known $\tilde{w}(X_r, \mu_r, \nu_r, t_0)$ and evolve the trajectories backward in time to $t' = t_0 - (t - t_0)$ according to (29) using different coordinates q [cf. Fig. 3(c)]. The desired $\tilde{w}(X_r, \mu_r, \nu_r, t)$ is then the sum over all such tomograms $\tilde{w}(X_q(t'), \mu_q(t'), \nu_q(t'), t_0)$, where the index q reflects the dependency on the parameters $\omega_0(q)$ and $q_c(q)$ in the propagator $\Pi_{\omega_0(q), q_c(q)}^T$.

An alternative approach which relates the time evolution of the quantum tomogram to the theory of Markov processes⁵³ has been considered recently²⁰. Interpreting the propagator Π^T as a transition probability for a Markov random process, its time evolution is governed by the Chapman-Kolmogorov equation⁵⁴

$$\Pi^T(z, t; z_0, t_0) = \int dz_\tau \Pi^T(z, t; z_\tau, \tau) \Pi^T(z_\tau, \tau; z_0, t_0), \quad (31)$$

where $t_0 < \tau < t$ and we introduced the abbreviation $z = (z^1, z^2, z^3) := (X, \mu, \nu)$. Due to the positivity of the tomogram and its normalization, the requirements

$$\Pi^T(z, t; z_0, t_0) \geq 0 \quad , \quad \int dz_0 \Pi^T(z, t; z_0, t_0) = 1 \quad (32)$$

for a Markov process are fulfilled. Furthermore, the locality in time of the Hamiltonian guarantees that no memory effects are present. The dynamics of diffusive Markov processes may be equivalently described by two partial differential equations, the first and the second Kolmogorov equation ⁵⁵,

$$\frac{\partial \Pi^T}{\partial t_0} + \sum_{i=1}^3 a^i(z_0, t_0) \frac{\partial \Pi^T}{\partial z_0^i} + \frac{1}{2} \sum_{i=1}^3 \sum_{j=1}^3 b^{ij}(z_0, t_0) \frac{\partial^2 \Pi^T}{\partial z_0^i \partial z_0^j} = 0, \quad (33)$$

$$\frac{\partial \Pi^T}{\partial t} + \sum_{i=1}^3 \frac{\partial}{\partial z^i} (a(z, t) \Pi^T) - \frac{1}{2} \sum_{i=1}^3 \sum_{j=1}^3 \frac{\partial^2}{\partial z^i \partial z^j} (b(z, t) \Pi^T) = 0, \quad (34)$$

in which the drift and diffusion coefficients are defined as

$$a^i(z_\tau, \tau) = \lim_{\tau' \rightarrow \tau} \frac{1}{\tau' - \tau} \int d\tilde{z}_{\tau'} \Pi^T(\tilde{z}_{\tau'}, \tau'; z_\tau, \tau) (\tilde{z}_{\tau'}^i - z_\tau^i), \quad (35)$$

$$b^{ij}(z_\tau, \tau) = \lim_{\tau' \rightarrow \tau} \frac{1}{\tau' - \tau} \int d\tilde{z}_{\tau'} \Pi^T(\tilde{z}_{\tau'}, \tau'; z_\tau, \tau) (\tilde{z}_{\tau'}^i - z_\tau^i) (\tilde{z}_{\tau'}^j - z_\tau^j). \quad (36)$$

In the limit $\tau' \rightarrow \tau$ we can evaluate (35) and (36) using the harmonic approximation Π_{ω_0, q_c}^T from (29). As the harmonic propagator depends on $\omega_0(q)$ and $q_c(q)$ of the local potential expansion, also the drift and diffusion terms are q dependent. For clarity of the notation, we will suppress the additional index for the moment.

Instead of solving (34) directly, we consider the equivalent system of stochastic integral equations ^{53,54} for the underlying random variables z ,

$$z^i(t) = z^i(t_0) + \int_{t_0}^t d\tau \psi(z_\tau, \tau) + \sum_{j=1}^3 \int_{t_0}^t d\tau g^{ij}(z_\tau, \tau) \xi^j(\tau). \quad (37)$$

Here $\xi^j(\tau)$ are white noise random processes with $\langle \xi^j(\tau) \rangle = 0$ and $\langle \xi^j(\tau) \xi^k(\tau') \rangle = \delta(\tau - \tau') \delta^{jk}$. For evaluating the second integral we will refer to the Stratonovich definition of a stochastic integral ⁵³. The functions $\psi(z_\tau, \tau)$ and $g^{ij}(z_\tau, \tau)$ relate to the drift and diffusion coefficients in (35) and (36) as

$$a^i(z_\tau, \tau) = \psi^i(z_\tau, \tau) + \frac{1}{2} \sum_{j=1}^3 \sum_{k=1}^3 \frac{\partial g^{ik}(z_\tau, \tau)}{\partial z_\tau^j} g^{jk}(z_\tau, \tau), \quad (38)$$

$$b^{ij}(z_\tau, \tau) = \sum_{k=1}^3 g^{ik}(z_\tau, \tau) g^{jk}(z_\tau, \tau). \quad (39)$$

For an implementation of the derivative term in (38) we profit from the equivalence ⁵⁴

$$\frac{1}{2} \sum_{j=1}^3 \sum_{k=1}^3 \frac{\partial g^{ik}(z_\tau, \tau)}{\partial z_\tau^j} g^{jk}(z_\tau, \tau) = \lim_{\Delta\tau \rightarrow 0} \frac{1}{\Delta\tau} \left\langle \sum_{k=1}^3 g^{ik}(\bar{z}_\tau, \tau) \Delta\xi_k(\tau) \right\rangle, \quad (40)$$

where $\langle \dots \rangle$ means the stochastic expectation value over the normalized Wiener process $\xi_k(\tau)$ and $\Delta\xi_k(\tau)$ is the corresponding increment of this random process in $\Delta\tau$. As a consequence of the Stratonovich integration the matrix elements g^{ik}

have to be evaluated at $\bar{z}_\tau = z_\tau + \frac{1}{2}\Delta z_\tau$, i.e., shifted by half the increment of z_τ during $\Delta\tau$. According to (39) these matrix elements can be calculated via Cholesky decomposition⁵⁶ from $b(\bar{z}_\tau, \tau)$. Note, that the matrix b is only positive semidefinite, requiring some care in the numerical determination of g , e.g, adding ε to b and taking the limit $\varepsilon \rightarrow 0$.

In summary, the evolution of a (X, μ, ν) trajectory is calculated iteratively from (37)-(40). To lowest order, in (37) only the deterministic drift term (35) is taken into account, which is evaluated using the local harmonic propagator (29). From the resulting increments $z(t) - z(t_0)$ we get a first estimate for b (and thus g) which we use in the next iteration. Having access to the deterministic part as well as the diffusion term in (37) we calculate several trajectories, needed for the expectation value in (40). Now an approximation for all terms in (37) is available and we can finally propagate our (X, μ, ν) trajectory. Alternatively, we can repeat the last step to ensure that the increments entering in (40) have been calculated using the full stochastic integral equation.

In addition to the stochastic character of the trajectory propagation, we have to keep in mind that the drift and diffusion terms depend on the coordinate at which (29) is evaluated. A suitable importance sampling of q is of crucial importance for an efficient implementation.

Although we discussed for simplicity only a three-dimensional vector $z = (X, \mu, \nu)$, which corresponds to one set of initial conditions, the generalization to k initial conditions directly carries over. In any case, including the initial condition for the coordinate representation is obligatory as a reconstruction of q out of z is necessary for intermediate evaluations of (29).

From the tomogram, general expectation values can be calculated in analogy to the Wigner function case²⁰. If the desired expectation value involves only position or momentum operators but not both, this task simplifies to an integration over the corresponding density. Let us consider for instance the kinetic energy $\frac{1}{2m}\langle p^2 \rangle$. With $\mu = 0$ and $\nu = 1$, the integral representation of the δ -distribution in (24) shows that $X \equiv p$ and we get

$$\frac{1}{2m}\langle p^2 \rangle = \frac{1}{2m} \int dX X^2 \tilde{w}(X, \mu = 0, \nu = 1) = \frac{1}{2m} \int dp p^2 |\psi(p, t)|^2. \quad (41)$$

2. Numerical Evaluation

As test cases for the above methods, we consider one-dimensional systems described by the Hamilton operators $H_i = \frac{p^2}{2m} + V_i(q)$. The four potentials

$$\begin{aligned} V_1(q) &= \frac{1}{2}m\omega_0^2 q^2 + V_0 \exp(-q^2) \quad , \quad V_2(q) = \frac{1}{2}m\omega_0^2 q^2 - V_0 \exp(-q^2) \\ V_3(q) &= \frac{1}{2}m\omega_0^2 (q^2 + a_3 q^4) \quad , \quad V_4(q) = V_0 + \frac{1}{2}m\omega_4^2 (-q^2 + a_4 q^4), \end{aligned} \quad (42)$$

shown in Fig. 4, each pose another numerical difficulty to semiclassical approaches. It is well known, that semiclassical methods perform well for harmonic or weakly

anharmonic cases, but that the effects of strong anharmonicities are hard to capture^{57,58}. Specifically, we chose $V_1(q)$ to study tunneling effects, $V_2(q)$ in view of resonances and $V_3(q)$ to investigate the influence of a nonlinear force term. Finally $V_4(q)$ combines the challenge of tunneling effects and anharmonicities in the potential. The inclusion of the shallow harmonic trap in $V_1(q)$ and $V_2(q)$ prevents the particle from escaping to infinity after the scattering event and restricts the simulation volume to a reasonable size. For all cases we use the same initial conditions, a Gaussian wave packet of width σ , centered at q_0 , with center momentum p_0 ,

$$\psi(q, t = 0) = \frac{1}{(2\pi\sigma^2)^{1/4}} \exp \left\{ -\frac{1}{4\sigma^2}(q - q_0)^2 + \frac{i}{\hbar}p_0q \right\}. \quad (43)$$

Taking the modulus squared $|\psi(q, t = 0)|^2$ of (43), the correct normalization to unity is obvious. Using the initial wave function (43) together with (18) we get the corresponding initial Wigner function

$$W(q, p, t = 0) = \frac{1}{\pi\hbar} \exp \left\{ -\frac{1}{2\sigma^2}(q - q_0)^2 - \frac{2\sigma^2}{\hbar^2}(p - p_0)^2 \right\}. \quad (44)$$

Comparing the coefficient of $(p - p_0)^2$ in the exponent to the standard form of a Gaussian, the standard deviation in momentum space reads $\sigma_p = \hbar/(2\sigma)$. Therefore, $\sigma\sigma_p = \hbar/2$, which makes our initial state a minimum uncertainty Gaussian wave packet. Integrating the Wigner function over the momentum (coordinate) variables, we get the probability density in coordinate (momentum) space,

$$|\psi(q, t = 0)|^2 = \int dp W(q, p, t = 0) = \frac{1}{\sqrt{2\pi\sigma^2}} \exp \left\{ -\frac{(q - q_0)^2}{2\sigma^2} \right\}. \quad (45)$$

It is clear, that we could have obtained this expression also directly by taking the modulus square of (43). To obtain the probability in momentum space,

$$|\psi(p, t = 0)|^2 = \int dq W(q, p, t = 0) = \sqrt{\frac{2\sigma^2}{\pi\hbar^2}} \exp \left\{ -\frac{2\sigma^2(p - p_0)^2}{\hbar^2} \right\}, \quad (46)$$

from the wave function, however, first a Fourier transform to momentum representation is necessary,

$$\begin{aligned} \psi(p, t = 0) &= \frac{1}{\sqrt{2\pi\hbar}} \int dq e^{-ipq/\hbar} \psi(q, t = 0) \\ &= \left(\frac{2\sigma^2}{\pi\hbar^2} \right)^{1/4} \exp \left\{ -\frac{\sigma^2}{\hbar^2}(p - p_0)^2 - \frac{i}{\hbar}q_0p + \frac{i}{\hbar}p_0q_0 \right\}. \end{aligned} \quad (47)$$

Finally, we obtain the tomograms of the initial state using (24) as

$$\tilde{w}(X, \mu, \nu, t = 0) = \frac{1}{\sqrt{2\pi\sigma_T^2(\mu, \nu)}} \exp \left\{ \frac{-(X - \mu q_0 - \nu p_0)}{2\sigma_T^2(\mu, \nu)} \right\}, \quad (48)$$

where the width of the tomogram σ_T depends on the particular reference frame (μ, ν) , and is given by

$$\sigma_T(\mu, \nu) = \sqrt{\nu^2 \left(\frac{\hbar}{2\sigma} \right)^2 + \mu^2 \sigma^2}. \quad (49)$$

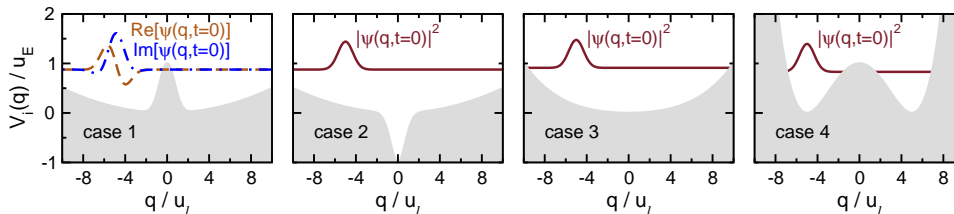


Fig. 4. From left to right: Benchmark potentials $V_i(q)$ as given by (42). The initial state in all cases is the same. For the first case we show the real and imaginary part of the wave function by dashed and dashed-dotted lines. In the other panels, the modulus square of the wave function is given. For comparison of the relevant energies, the baseline of the wave function is drawn at the energy of the initial state.

Throughout this work we express all quantities in terms of the fixed reference units for length (u_ℓ), mass (u_m) and time (u_t). From those we may also construct units for energy ($u_E = u_m u_\ell^2 / u_t^2$) and momentum ($u_p = u_m u_\ell / u_t$). In these units $\hbar = u_m u_\ell^2 / u_t$. To be specific, in (42) we use $m = u_m$, $\omega_0 u_t = 0.1$, $a_3 u_\ell^2 = 0.01$, $\omega_4 u_t = 0.4$, $a_4 u_\ell^2 = 0.02$ and $V_0 = u_E$. As initial conditions, we choose $q_0 = -5u_\ell$, $p_0 = u_p$ and $\sigma = u_\ell / \sqrt{2}$.

2.1. Discussion of the time evolution

Probability densities Figure 5 shows the time evolution of the probability density in coordinate space, $|\psi(q,t)|^2$, for times up to $t = 56u_t$. Each column corresponds to one of the above potentials (42) while the rows refer to the methods used. The topmost row, calculated by Chebyshev expansion (C), gives the exact solution. For the barrier case [$V_1(q)$, first column] the particle hits the barrier (center position marked by a dashed line), at about $t \approx 5u_t$. Here, the main part of the wave packet is reflected, but a sizeable fraction also penetrates through the barrier. The quantum nature of the particle gives rise to the interference pattern on the left hand side of the barrier, where high and low probability densities alternate. This effect is still more pronounced around $t \approx 35u_t$ when the transmitted and reflected parts interfere after their reunion. For the case of a quantum well [$V_2(q)$, second column], we observe the overall picture expected for the dynamics in a simple harmonic trap. Since the width of the initial Gaussian, however, does not match the resonance frequency of the harmonic trap, its width changes during the time evolution, refocusing once each π/ω_0 . The rather small effect of the additional dip at $q = 0$ consists in a reduced density in this region for all times and a retardation of the transmission. For the case of an anharmonic potential [$V_3(q)$, third column], besides the above mentioned broadening of the wave packet, the nonlinearity of the force causes additional interference effects. Elongations up to $q \approx 15u_\ell$, exceeding the classical turning points $q_c \approx 8.2u_\ell$, are possible due to the quantum nature of the initial state. Despite its fixed total energy, the initial wave packet contains contributions with higher and lower energies. The fourth column shows the rich structure of the

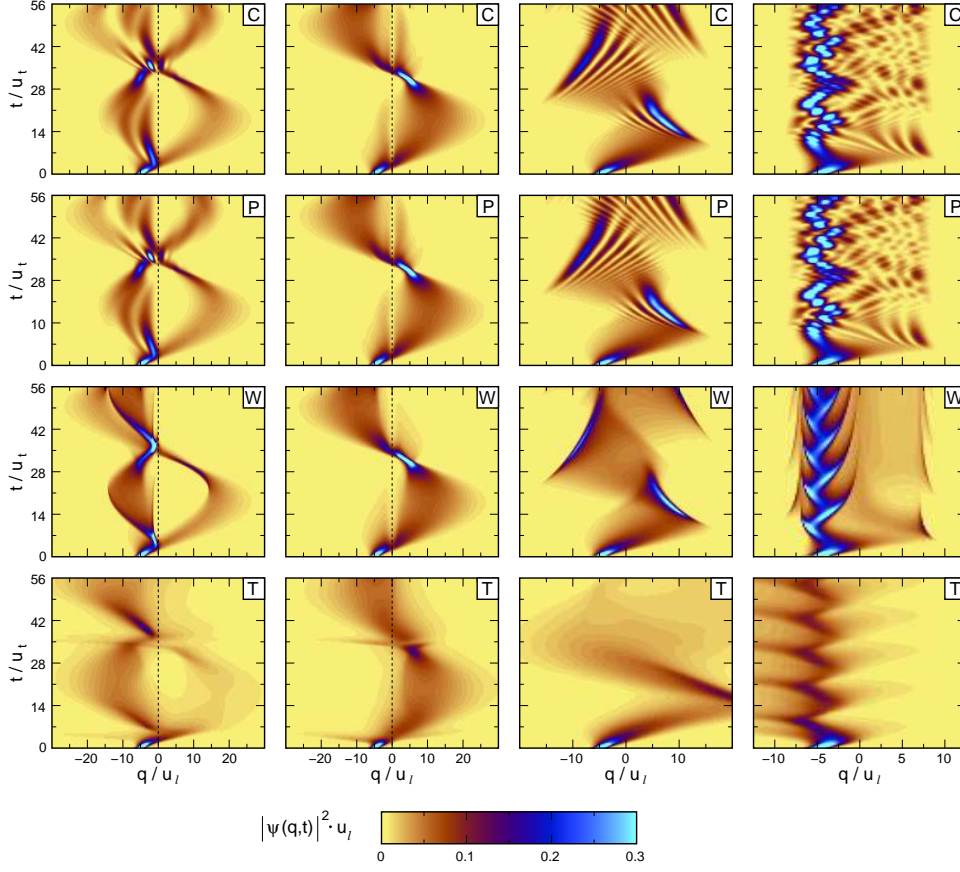


Fig. 5. From left to right: Time evolution of the probability density in coordinate space, $|\psi(q,t)|^2$, for a particle in the benchmark potentials $V_1(q)$ to $V_4(q)$ as given by (42). For each case, we show (from top to bottom) the exact solution, calculated by Chebyshev expansion (C), the results from the linearized semiclassical propagator method (P), the results from the first order Wigner-Moyal approach (W) and the tomographic results (T). For implementation details see Sect. 2.2.

dynamics in the double well potential. While the principle part of the wave function remains in the left well, a considerable amount penetrates the barrier where strong interference effects arise. The back scattering of these contributions causes strong interference patterns also in the left well for $t > 10u_t$.

In the second row, the results from the linearized semiclassical propagator method (P) fully coincide with the exact results. The excellent agreement confirms, that within a semiclassical framework it is in principle possible to capture quantum effects, although by an tremendous increase of computational resources (cf. Sect. 2.2).

Restricting the iteration series for the Wigner function to first order, we obtain the results shown in the third row (W). The initial splitting of the wave packet for the barrier case $V_1(q)$ at about $t \approx 5u_t$ is reproduced while the second one around

$t \approx 35u_t$ is missed. The explanation of this failure is simple. Trajectories with high enough energy to cross the barrier once will be able to cross it any time, oscillating forth and back in the trap potential. Others which already failed the first passage due to an insufficient energy are reflected every time they hit the barrier. Hence they stay on the left side of the barrier for all times and in the second half period, $t > 35u_t$, there is almost no spectral weight to the right of the barrier. Nevertheless some, exponentially rare, trajectories can be found there. Large negative initial momenta make some trajectories energetic enough to overcome the barrier, but lead to a phase shift as compared to the trajectories with positive initial momentum. Furthermore, the first order Wigner results fail to resolve the fine structure of the interference effects for $V_3(q)$ and $V_4(q)$. In this sense, the quantum information contained in this approximation is limited even though in the initial Wigner function $W_0(q, p, t_0)$ all quantum effects (to arbitrary high orders of \hbar) are included. As we will see later, taking into account the second order term of the iteration series will alleviate these problems.

The bottom line shows the results from the tomographic approach (T). Here, the positions for the potential evaluation in (29) are calculated from classical trajectories sampled from the initial distribution. While also here, the dynamics of the system is described qualitatively, there is nevertheless a large discrepancy to the exact data. Four weak points should be stressed. First, any sharp feature in $|\psi(q, t)|^2$ is washed out even more than in the Wigner approach. Second, for $V_1(q)$ and $V_2(q)$, the signatures at $t \approx 5u_t$ erroneously extend to too large negative q -values. The reason for this are diverging trajectories, caused by the negative curvature of the barrier potential. Third, the turning points in the anharmonic potentials ($V_3(q)$ and $V_4(q)$) are highly overestimated, which is an effect of the coordinate sampling for the potential evaluation. Forth, the tunneling in the double well potential is not accounted for correctly. This is due to the large range of q for which the curvature of the potential is negative. Hence, the amount of rejected trajectories is overestimated.

Expectation values The semiclassical propagation of the Wigner function and the tomogram is intended to give an adequate description of complex many particle systems. Thereby, average values take the center stage.

For the potentials $V_{\{1,2,4\}}(q)$ the initial wave packet splits in two parts. To account for this in terms of expectation values, we define reduced average quantities for the positive and negative half-axis,

$$\langle q \rangle_- = \frac{1}{N_-} \int_{-\infty}^0 q |\psi(q, t)|^2 dq \quad , \quad \langle q \rangle_+ = \frac{1}{N_+} \int_0^{\infty} q |\psi(q, t)|^2 dq \quad , \quad (50)$$

where N_{\pm} is the partial norm on the corresponding half-axis,

$$N_- = \int_{-\infty}^0 |\psi(q, t)|^2 dq \quad , \quad N_+ = \int_0^{\infty} |\psi(q, t)|^2 dq \quad . \quad (51)$$

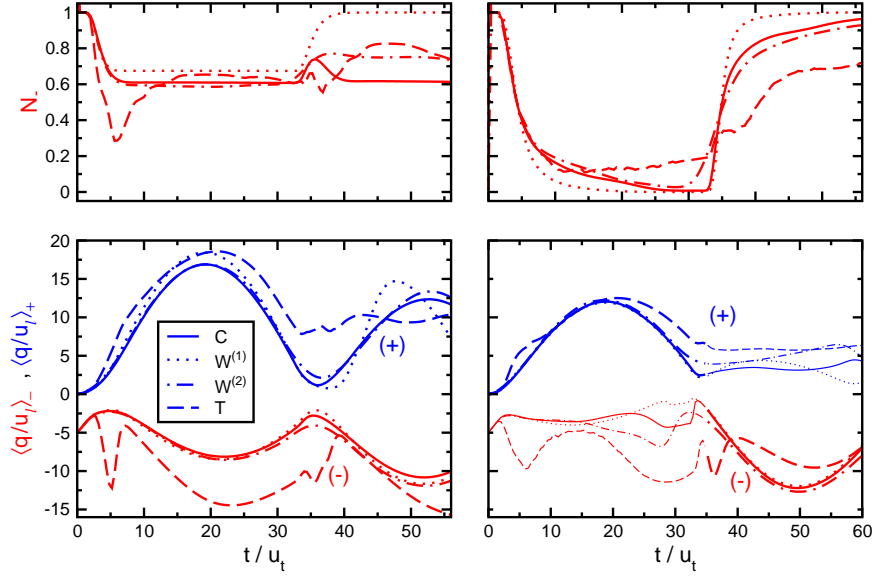


Fig. 6. Expectation values for the benchmark potentials $V_1(q)$ (left column) and $V_2(q)$ (right column). The upper panels show the part of the wave function norm on the negative half-axis N_- . In the lower panels, the mean positions $\langle q \rangle_{\pm}$ on the corresponding half-axis are given. We show the exact results from the Chebyshev expansion (C – solid lines) as well as the first and second order approximations from the Wigner-Moyal approach ($W^{(1)}$ – dotted lines; $W^{(2)}$ – dashed-dotted lines) and tomographic results (T – dashed lines). As the wave functions obtained by the semiclassical propagator method agree within numerical accuracy with the exact results from C , no separate curves are shown.

For the first two test cases, we show in Fig. 6 the time evolution of the initial state in terms of $\langle q \rangle_{\pm}$ and N_- . The norm on the positive half axis is not shown separately as $N_+ = 1 - N_-$. For $V_1(q)$, the constant value of N_- after the initial tunneling event ($t \approx 5u_t$) indicates an independent evolution of the two wave packets on their corresponding half-axis. Only at the refocusing point ($t \approx 35u_t$) weight is temporarily redistributed between them due to interference effects. From $\langle q \rangle_{\pm}$, the oscillation between the barrier and the confining trap of each wave packet can be identified. The mean energy of the transmitted wave packet is larger than for its reflected counterpart as the mean position reaches larger values. Quantum dynamics, however, comprehends more than a simple energy discrimination of the constituents of the wave packet by the barrier.

This becomes obvious when considering the first order Wigner result, $W^{(1)}$. Containing the classical energy discrimination only, the finite value of N_+ for $t > 35u_t$ is missed as already discussed in Fig. 5. The ratio of N_+ to N_- within this approximation is solely determined by the initial energy of each simulated classical trajectory. Those constituents of the initial state with $E > V_0$ will overcome the barrier while others will not. For an estimate, we calculate the energy of the initial state, neglecting for simplicity the influence of the barrier. Then N_- (N_+) is

the integral over the initial Wigner function inside (outside) an ellipse defined by $p^2/(2m) + \frac{1}{2}m\omega_0^2q^2 = V_0$. This result agrees well with the numerical data. The strong underestimate of N_+ for $t > 35u_t$ within $W^{(1)}$ explains the deviation of $\langle q \rangle_+$ in this range.

Taking into account the second order term of the iteration series, $W^{(2)}$, slightly improves the accuracies of both the norm and the reduced expectation values; the relative weight of the split wave packet (N_-) after $t > 35u_t$ still deviates about 15% from the exact value. This deviation is related to the finite grid resolution, smearing out the exact positions during the recurrent coordinate sampling and grid deposition. Increasing the grid resolution, this effect can be reduced systematically.

In the tomographic approach, the focus on expectation values does not resolve the problems encountered for the probability density. Around $t \approx 5u_t$, when mainly the barrier region is sampled, we observe two consequences of the negative potential curvature. On the one hand, the fraction of trajectories which overcome the barrier is overestimated (too small value of N_-). On the other hand, a considerable amount of the reflected trajectories diverges and thus the value of $\langle q \rangle_-$ is too negative. Apart from this the expectation values reproduce the results of C qualitatively but not quantitatively. Here the especially remarkable features are the larger elongation of $\langle q \rangle_-$ and the absence of a pronounced modulation of $\langle q \rangle_+$ for $t > 35u_t$.

For $V_2(q)$ (right column) the norm indicates the nearly perfect transmission of the wave packet since for each time there is considerable weight on one half-axis only. Therefore, the average positions show an almost perfect sinusoidal oscillation, if we consider $\langle q \rangle_+$ for $t < 35u_t$ and $\langle q \rangle_-$ afterwards (thick parts of the solid lines). On the respective other half-axis the average values should be taken with care due to the low weight. The rather good agreement between the expectation values from C and $W^{(1)}$ in this case is not surprising. It is known from the literature that for harmonic potentials the exact Wigner function can be obtained by classical propagation of trajectories¹³. As the dip around $q = 0$ is only a moderate perturbation, $W^{(1)}$ describes the dynamics still well. For this case, also the method of Wigner trajectories^{59,60,61} is applicable, in which the higher order terms of the iteration series are included perturbatively into a pseudopotential $\tilde{V}(q)$. The trajectories then follow the classical equations of motion with respect to $\tilde{V}(q)$ instead of $V(q)$. For the construction of such a pseudopotential an approximate Wigner function is required. This limits a practical application of the method of Wigner trajectories to slightly perturbed harmonic potentials or nearly free motions¹³. Furthermore, the existence of $\tilde{V}(q)$ is not guaranteed due to the perturbative character of this scheme. Since for this potential the $W^{(1)}$ results for $\langle q \rangle_{\pm}$ almost perfectly match C for the majority branch, the profit in considering $W^{(2)}$ is limited. Merely in the time evolution of N_- an improvement from $W^{(1)}$ to $W^{(2)}$ is noticeable. The tomographic results once more show a qualitative agreement with C . In addition to the deviations for the minority branch, the diverging trajectories, arising when the wave packet crosses the dip, perturb the results around $t/u_t \approx 5, 35$.

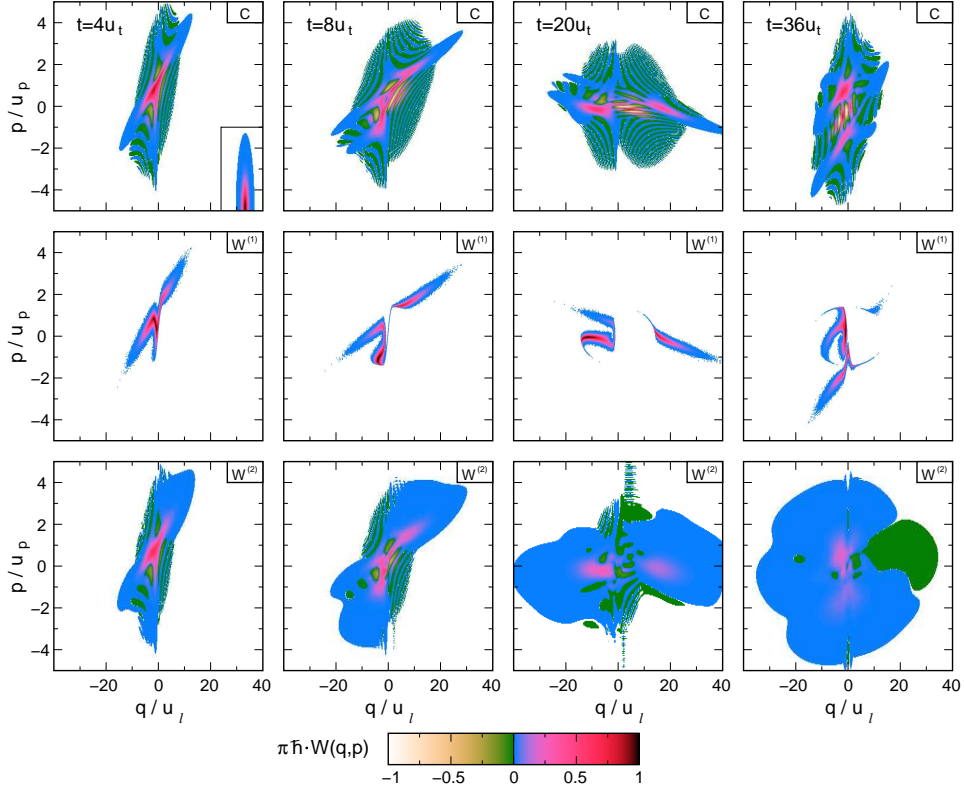


Fig. 7. Time evolution of the Wigner function for potential $V_1(q)$. Upper panels: Exact result using Chebyshev expansion (C). Middle panels: Propagation of the initial Wigner function using classical trajectories only [first order approximation, $W^{(1)}$]. Lower panels: Inclusion of momentum jumps [second order approximation, $W^{(2)}$]. For each method snapshots at times $t/u_t = 4, 8, 20, 36$ are shown. For comparison, the inset in the upper left panel shows the extension of a minimum uncertainty Gaussian.

Wigner function Focusing on the barrier case, $V_1(q)$, we compare in Fig. 7 the exact Wigner function, calculated from the (Chebyshev propagated) wave function together with definition (18), to the first and second order approximation. The extension of a minimum uncertainty Gaussian (inset in upper left panel in Fig. 7) is the lower limit where the concept of a joint probability holds due to the Heisenberg uncertainty relation. Nevertheless, comparing $W(q, p)$ for different approximations can be taken as a good quality check since any observable of the system is obtained as an integral over the Wigner function. Starting from the initial Wigner function (Gaussian, centered at $q = -5u_\ell$, $p = u_p$), the overall time evolution is dominated by a clockwise rotation of the phase space points. When the fastest contributions of the wave packet encounter the barrier ($t = 4u_t$), for the first time significant negative values of $W(q, p)$ occur. The initial Gaussian shape breaks up into a triangle, reflecting the low-energy trajectories which are held back by the barrier and

the fast contributions overcoming the barrier. The quantum nature is reflected in a weak interference pattern of small positive and negative values around the main structure. Evolving further in time ($t = 8u_t$), the regions with negative weights get more pronounced. At $t = 20u_t$ there is a strong interference pattern of large positive and negative values of $W(q, p)$ in between the two major positive portions left and right of the barrier. When the transmitted part returns to the left side of the barrier ($t = 36u_t$) the structure remains divided with strong interference in between the two positive bulks.

Considering the first order approximation, the most pronounced difference compared to the full quantum result is the absence of regions with negative values in $W^{(1)}$. This is clear as the initial state $W(q, p, t = 0)$ is strictly positive and during the classical propagation of the trajectories their weight is unchanged. Therefore, at any time $W^{(1)}$ is a superposition of positive contributions. Despite the simplicity of this approximation, all regions with large positive weights are in essence captured correctly. Regions of nearby positive and negative values in the exact solution are marked within $W^{(1)}$ by vanishing, or strongly reduced values (cf. $q/u_\ell \in [0, 10]$, $p/u_p \in [-1, 1]$ at $t = 20u_t$). The integral over p in this region vanishes for both $W^{(1)}$ and the exact solution, explaining why physically measurable quantities like $|\psi(q, t)|^2$ agree well despite the differences in $W(q, p)$.

Including the second order term of the iteration series, the presence of negative weights is restored in $W^{(2)}$. Even though, arbitrarily large momentum jumps are allowed for the trajectories, finite amplitudes of $W^{(2)}$ are restricted to the center region. Outside this region, the fast oscillations of $\omega(s, q_\tau)$ guarantee the complete cancellation present in the exact results. Taking the finite simulation grid into account, the extent of this cancellation will delicately depend on the used resolution and accuracy of the (MC) integration. A signature of a non-perfect cancellation can be seen for $t = 20u_t$ at values of $q/u_\ell \in [5, 10]$ and large p as a series of positive and negative stripes. Accumulating such numerical fluctuations, the true region with finite amplitudes is overestimated for large times ($t = 36u_t$).

2.2. Details of implementation

Chebyshev expansion In view of further applicability of the proposed methods, let us focus on the computational requirements in what follows. In this regard, the description of quantum dynamics by Chebyshev expansion of the time evolution operator is an extremely powerful method. Its extraordinary performance is not restricted to the one-dimensional test cases considered here, but has been demonstrated successfully for more complex, higher dimensional cases^{62,63}. Despite the exponential growth of the Hilbert space with the number of particles, also an application to many-particle systems, e.g., the polaron problem is within reach²⁵. As compared to the standard Crank-Nicholson algorithm⁵⁶, the Chebyshev expansion has two main advantages: speedup and larger accessible system sizes. First, for the Chebyshev expansion only MVM are required, while for the Crank-Nicholson

scheme,

$$\left(1 + \frac{1}{2}iH\Delta t/\hbar\right) |\psi(t_0 + \Delta t)\rangle = \left(1 - \frac{1}{2}iH\Delta t/\hbar\right) |\psi(t_0)\rangle, \quad (52)$$

a linear equation system needs to be solved in each time step. While for the one-dimensional case considered here, the tridiagonal structure of the coefficient matrix speeds up the calculation, in general the solution of this system is the most time consuming step. Speeding up the calculation by an initial inversion of the time independent coefficient matrix and performing successive MVM afterwards is only feasible for moderate Hilbert space dimensions.

Second, the Crank-Nicholson algorithm is accurate to order $(\Delta t)^2$, whereas the accuracy of the Chebyshev expansion is determined by the expansion order M . We may choose M such that for $k > M$ the modulus of all expansion coefficients $|c_k(a\Delta t/\hbar)| \sim J_k(a\Delta t/\hbar)$ is smaller than a desired accuracy cutoff. This is facilitated by the fast asymptotic decay of the Bessel functions,

$$J_k(a\Delta t/\hbar) \sim \frac{1}{\sqrt{2\pi k}} \left(\frac{ea\Delta t}{2\hbar k}\right)^k \quad \text{for } k \rightarrow \infty. \quad (53)$$

Then, for large M , the Chebyshev expansion can be considered as quasi-exact and thus permits a considerably larger time step. For example, using a simulation grid of $N = 1024$ sites with grid spacing $\Delta\tilde{q} = 0.08u_\ell$ the necessary scaling parameters for the four test cases are $a = 160, 161, 226, 2307$, and for $k > M = 108, 108, 140, 1028$ all $|c_k| < 10^{-16}$. These cutoffs ensure that the wave function is exact for the used time step $\Delta t = 0.4u_t$ for all times. Here, ‘exact’ means that within numerical accuracy the wave function agrees with the time dependent wave function obtained by a full diagonalization of the Hamiltonian,

$$|\psi(t)\rangle = \sum_{n=1}^N e^{-iE_n t/\hbar} |n\rangle \langle n|\psi(t=0)\rangle, \quad (54)$$

where $|n\rangle$ are the (time independent) eigenstates of the system and E_n the corresponding eigenenergies.

Besides the high accuracy of the method, the linear scaling of computation time with both time step and Hilbert space dimension are promising in view of further applications to more complex systems. Almost all computation time is spent in MVMs, which can be efficiently parallelized, allowing for a good speedup on parallel computers.

Linearized semiclassical propagator method The considered implementation of the linearized semiclassical propagator method is not intended for a fast determination of an approximate solution. In this respect, more efficient flavors of semiclassical propagator methods can be found in the literature, where higher order potential terms are taken into account and the propagated trajectories are chosen by some kind of importance sampling. Instead, we focus on the question how close

a semiclassical approximation can be to the exact quantum solution if we let all concerns about computational requirements aside. To achieve the desired accuracy, two aspects are of prominent importance. First, we cannot choose the trajectories that have to be propagated solely according to the current wave function amplitude at the grid points. For the overall interference effects, also trajectories starting at grid points with low amplitudes are of importance. Already discarding trajectories with initial weight $|\psi(q_0, t_0)| < 10^{-6}$ influences the interference pattern and leads to a noticeable deviation from the exact results in phase and also magnitude. Second, the used time step has to fulfill the Courant criterion²⁸. During a single time step any trajectory has to stay within its initial grid cell to ensure the validity of the local potential approximation. Fortunately, the maximum distance a trajectory may cover in one time step can be calculated exactly to optimize the time step. From (16) we read the displacement in one time step Δt as $\Delta q = -s(\Delta t)^2/(2m) + p_0\Delta t/m$. Substituting the largest value for $|p_0| = \pi\hbar/(\Delta\tilde{q})$ and requiring $|\Delta q| < \Delta\tilde{q}/2$, the maximum time step is given by

$$\Delta t_{\max} = \frac{\pi\hbar}{|s|\Delta\tilde{q}} \left(\sqrt{1 + \frac{|s|(\Delta\tilde{q})^3 m}{\pi^2\hbar^2}} - 1 \right). \quad (55)$$

As for the reconstruction of the wave function contributions from the whole grid are necessary, the grid points with the largest slope s will be most restrictive for the time step. For $V_1(q)$ to $V_4(q)$ the used time steps are $\Delta t/u_t = 5 \times 10^{-3}, 5 \times 10^{-3}, 5 \times 10^{-4}, 10^{-4}$ on grids with $N = 1024, 1024, 512, 256$ sites and grid spacing $\Delta\tilde{q} = 0.125u_\ell$. Using those parameters, the results reproduce within numerical accuracy the results from the full quantum calculation, including the correct phase of the wave function.

Wigner-Moyal-approach The numerical demands of directly propagating the Wigner function depend drastically on the order of the iteration series taken into account. For $W^{(1)}$, the classical propagation and assembly of a large number of paths ($N_p \approx 10^7$) is possible at very low computational costs. The continuity of the phase space trajectories allows for once sampling the initial conditions and then following those paths up to arbitrary times. In contrast, for higher order approximations a single initial sampling is not sufficient anymore. Due to momentum jumps also regions far away from the classical end points acquire a finite weight. Then, a resampling of the initial conditions at each time grid point is necessary. Performing such a resampling also for $W^{(1)}$ slightly influences the data shown in Fig. 7. While for short times the agreement is almost perfect, with increasing time the sharp features present in the continuous results are washed out by the resampling. Caused by the grid discretization this effect systematically decreases with the used number of grid points. The shape function used in the deposition to the grid influences the necessary number of trajectories to achieve a desired accuracy. Using the ‘cloud-in-cell’ (CIC) scheme²⁸, weight is attributed to the two nearest grid points in each direction, constituting a reasonable compromise between deposition costs

and necessary broadening. For the first order results shown in Figs. 5 - 7 we used $N_p = 10^7$ initially sampled trajectories. Those are deposited by the CIC scheme onto a 400×400 grid with $\Delta\check{q} = 0.225u_\ell$ and $\Delta\check{p} = 0.045u_p$.

For $W^{(2)}$, the computational requirements increase drastically. While the recipe how to implement this order approximation is straight forward, improving the accuracy as compared to the first order results is numerically challenging. Especially the stability of the long time evolution depends drastically on several factors. First, in each time step the MC sampling of the initial conditions depends on the previous result. Therefore, numerical and statistical fluctuations may amplify in runs with too poor statistics. As for the considered one-dimensional systems a direct integration is feasible, we refrain from the MC integration to circumvent possible convergence problems. Adapting Fig. 2 to the full integration scheme, the considered initial phase space points (q_0, p_0) cover the whole (\check{q}, \check{p}) grid. As long as $t - t_0$ is not too large, the τ -integral can be evaluated by the midpoint rule. In absence of momentum jumps the classical trajectory evolves continuously in $[t_0, t]$. As compared to the dependency on the magnitude of the momentum jump occurring at τ the influence of the exact jumping time τ in $[t_0, t]$ is of minor importance. Working on a fine s grid, at τ all those momentum jumps are performed for which the final position (q_τ, p_τ) does not exceed the simulation grid. From the updated phase space point, the corresponding trajectories are then evolved up to time t , where they are deposited onto the (\check{q}, \check{p}) grid by means of the CIC scheme. Second, for the calculation of $\omega(s, q_\tau)$ the derivative of the δ -distribution in (20) needs to be implemented numerically. Approximating the δ -distribution by a Gaussian of width σ_δ , the corresponding derivative reads

$$\frac{d\delta}{ds} = \lim_{\sigma_\delta \rightarrow 0} \left[-\frac{s}{\sqrt{2\pi\sigma_\delta^3}} \exp\left(-\frac{s^2}{2\sigma_\delta^2}\right) \right]. \quad (56)$$

Taking into account the finite resolution of the simulation grid, a finite value of σ_δ is necessary despite the desired limit $\sigma_\delta \rightarrow 0$. In the calculation we use $\sigma_\delta = \Delta\check{p}$ and choose the resolution of the momentum jump grid as $\Delta\check{s} = 0.1\Delta\check{p}$ in order to resolve the structure of $d\delta/ds$ in the s integration. A further reduction of σ_δ (and an according refinement of the momentum jump grid) does not increase the quality of the results. In addition, the maximum allowed time step has to be severely reduced to prevent numerical instabilities due to the increased $\omega(s, q_\tau)$ values in the vicinity of $s = 0$. For the relevant range of s and q_τ the function $\omega(s, q_\tau)$ is shown in Fig. 8 for $V_1(q)$ to $V_4(q)$. Using the same phase space grid as for the first order approximation, the time step $\Delta t = t - t_0 = 0.04u_t$ fulfills the stability requirements for the chosen value of $\sigma_\delta = \Delta\check{p}$.

Tomographic approach The crucial point of the tomographic approach is a suitable sampling of the potential landscape entering (29). A straight forward implementation of (30) suggests the consideration of the whole coordinate axis for each time step and each trajectory (X, μ, ν) . Then depositing each varied Gaussian onto

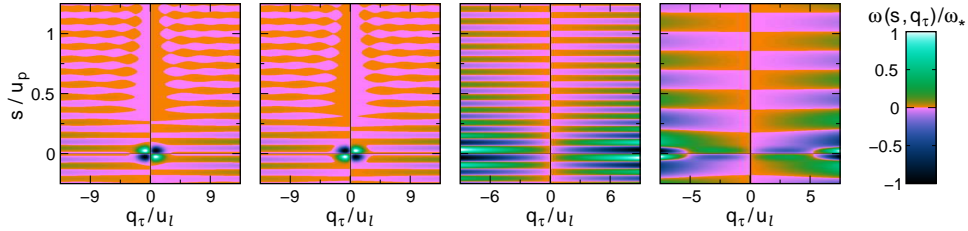


Fig. 8. Weighting function $\omega(s, q_\tau)$ in (22) for the potentials $V_1(q) - V_4(q)$ (left to right). The shown functions $\omega(s, q_\tau)$ are normalized to $\omega_* u_m u_\ell = 300$ (450) for the potentials $V_{\{1,2\}}(q)$ ($V_{\{3,4\}}(q)$). The derivative of the δ -distribution is implemented according to (56) with $\sigma_\delta = \Delta \tilde{p} = 0.045 u_p$. Note that the oscillation period in s direction is influenced by the range of considered q_τ and q' in the integration (22). Here we used $|q'/u_\ell|, |q_\tau/u_\ell| < 30, 30, 30, 10$.

the coordinate axis to obtain $|\psi(q, t)|^2$, such an implementation would be closely related to the concept of Sect. 1.2. The main difference between both methods is the more complicated propagation of the individual trajectories in the tomographic approach. Using a local harmonic instead of a linear expansion of the potential and including a diffusive term allows this method to use a larger time step. But the computational overhead caused by the complexity of the calculation of each time step clearly outweighs this profit.

Exploiting the major advantage of the tomogram – its positivity – calls for choosing the used coordinates by a MC procedure instead. A direct sampling of the coordinates according to the current probability density $|\psi(q, t)|^2$, however, fails completely to reproduce the exact results. Instead of the splitting, only a diffusive broadening of the initial wave packet is observed for $V_1(q)$. Apparently no trajectories overcome the barrier as in (29) only the repulsive force from the potential but not the actual momentum distribution is taken into account. To include the interplay between potential and momentum, for the data presented in Figs. 5 and 6 we evaluate the potential at the positions of simultaneously propagated auxiliary trajectories. Starting from a phase space point (q, p) , sampled from the initial (quantum) state, they are classically propagated in time. Note that the auxiliary trajectories determine the potential entering in (30), but the evolved tomogram exerts no back action on them. Thus (X, μ, ν) , and correspondingly the center of the varied Gaussian for the deposition of $|\psi(q, t)|^2$, may significantly deviate from the auxiliary trajectory, especially if the potential is evaluated in a region of negative curvature. The diverging signatures around $t/u_t = 5, 35$ for $V_1(q)$ are due to auxiliary trajectories with energies of almost exactly V_0 . Those stay in the negative curvature region in the vicinity of the potential maximum for a long time. There the evolution of (X, μ, ν) is governed by hyperbolic functions in (29).

Apart from this, the pronounced smoothing of the results in Fig. 5 is striking. The broadening during the time evolution results from the dependency of the width of the deposited Gaussians on (X, μ, ν) , spoiling a good resolution. On the other hand, approximate results are accessible with much less ($N_p = 12000$) trajectories

than for the other discussed semiclassical methods. Controlling the steadily increasing width of the Gaussians requires some kind of restarting procedure in which the tomogram is resampled by Gaussians of unit width after a certain time. Performing such a resampling at each time grid point, we again approach the concept behind Sect. 1.2. Declining such a restarting procedure in this work, the given results demonstrate the limitation of the tomographic approach when sampling the auxiliary trajectories only once.

3. Conclusion

In this work, we have compared different semiclassical approaches to quantum mechanics regarding their numerical implementation and efficiency. Focusing on the time evolution of a wave packet in one-dimensional quantum structures, we studied tunneling, interference and nonlinearity effects. Results were obtained for the probability density and various expectation values and contrasted against the exact quantum mechanical solution, calculated by means of a Chebyshev expansion technique. The Chebyshev method is fast, numerically stable and therefore perfectly suited to resolve the full dynamics of a quantum system. Accessible system sizes are much larger than the ones that can be reached by other direct solution schemes of the time-dependent Schrödinger equation (e.g., using the Crank-Nicholson algorithm or full diagonalization).

A brute force implementation of the Feynman path integral can be performed by adapting a linearized semiclassical propagator method, where the inclusion of ‘all possible paths’ is traced back to the set of possible initial conditions on a discrete coordinate and momentum grid. Having in mind that within this approach the computation time scales as $N^2 N_t$, where N (N_t) is the number of space (time) grid points, the applicability to more complex systems is obviously limited. Instead, the implementation should be considered as a ‘proof of principle’ that quantum effects are accounted for correctly if one takes into account the complete superposition of the complex weighted trajectories within a local linear approximation of the potential. Implementations going beyond this linear potential approximation require a full inclusion of the monodromy matrix. If one, along this line, correctly takes into account any phase jumps at the focal points, the time step may be increased without loss of accuracy. On the other hand, the neglect of some trajectories by the MC sampling procedure of the initial conditions leads to a systematic loss of accuracy.

Adopting a probabilistic point of view, the Wigner representation of quantum mechanics offers an alternative approach to quantum dynamics. In the Wigner-Moyal scheme the Wigner function is propagated in time according to an equation of motion, being equivalent to the von Neumann equation. We transform this equation of motion into an integral equation which can be solved in terms of an iteration series. Then, to leading (first) order, classical trajectories are propagated in time. Thereby their initial conditions are sampled from the initial Wigner function. Here,

the low computational costs outweigh the loss of some aspects of quantum dynamics. Trying to improve the quality of the approximation by including the next (second) order term of the iteration series, we are faced with a tremendous increase of computation time. This is due to the necessity of considering a large number of trajectories, a high resolution of the phase space grid and a correspondingly small time step, in order to avoid the amplification of numerical fluctuations. Thus, in order to get the exact quantum mechanical results, we need an even higher numerical effort than for the linearized semiclassical propagator method. Contrasting the Wigner function results of both orders, the gain in accuracy for the second order scheme is only moderate such that the additional computational overhead seems not justified. Hence, the complexity of the implementation and the ill posed numerics impede the application of the higher order Wigner-Moyal approach to the description of more complex systems.

Finally, the tomographic representation of quantum mechanics aims at describing quantum dynamics in terms of a positive semidefinite function. The quantum tomogram can be interpreted as a set of Radon transformations of the Wigner function. Relating its time evolution to a diffusive Markov process, the dynamics of the system is governed by a set of stochastic integral equations derived from the Kolmogorov equations for the tomogram. In the calculation of the drift and diffusion coefficients for the stochastic differential equations, we used the harmonic propagator deduced from a local, second order approximation of the potential. The sampling of the potential landscape is the crucial point of this method and strongly influences the quality of the data. Evaluating the potential at the coordinates of classically evolving trajectories, we reproduce the quantum results qualitatively but not quantitatively. As compared to the other considered semiclassical approaches, the quality of the data is poor, especially for potentials with distinct negative curvatures. We expect a noticeable improvement of the results only if a more efficient sampling of the coordinates for the potential evaluation can be found. With respect to the computational costs, the tomographic approach is slightly more expensive than the Wigner-Moyal approach in first order approximation but much faster than the linearized semiclassical propagator method or the Wigner-Moyal approach in second order.

To summarize, although the above analyzed semiclassical methods in principle capture all quantum effects, they largely differ in quality and required computational costs. If one is interested in a method to include minor quantum corrections on top of a classical description, the first order Wigner approach is best suited as it provides a reasonable compromise between accuracy and computation efficiency. Of course, it is possible to reproduce the complete quantum mechanical solution at the expense of a dramatic increase of the computing resources. In this respect, the linearized semiclassical propagator method is slightly more efficient than the second order Wigner approach. While more quantum effects should be included in the tomographic than in the first order Wigner description, the expectation values obtained by the former approach are not as good as expected. These aspects

have to be kept in mind when applying the above methods to the time evolution of more complex systems.

Acknowledgments

This work was supported by the DFG through the research program SFB TR 24, the Competence Network for Technical/Scientific High-Performance Computing in Bavaria (KONWIHR) and the Helmholtz-Gemeinschaft through COMAS. We thank M. Bonitz, D.E. Dauger, V.K. Decyk, A.V. Filinov, V.E. Fortov, P. Levashov and J. Tonge for helpful discussions. The numerical calculations have been performed on the TeraFlop compute cluster at the Institute of Physics, Greifswald University.

References

1. H. Fehske, A. Weiße, R. Schneider (Eds.), Computational many-particle physics, Vol. 739 of Lecture Notes in Physics, Springer, Berlin Heidelberg, 2008.
2. I. Peschel, X. Wang, M. Kaulke, K. Hallberg (Eds.), Density-matrix renormalization. A new numerical method in physics., Vol. 528 of Lecture Notes in Physics, Springer-Verlag, Heidelberg, 1999.
3. E. Jeckelmann, H. Fehske, Exact numerical methods for electron-phonon problems, *Rivista del Nuovo Cimento* 30 (2007) 259.
4. W. H. Miller, The semiclassical initial value representation: a potentially practical way for adding quantum effects to classical molecular dynamics simulations, *J. Phys. Chem. A* 105 (2001) 2942.
5. M. Thoss, H. Wang, Semiclassical description of molecular dynamics based on initial-value representation methods, *Ann. Rev. Phys. Chem.* 55 (2004) 299.
6. W. H. Miller, Classical S-matrix: numerical application to inelastic collisions, *J. Chem. Phys.* 53 (1970) 3578.
7. M. V. Berry, K. E. Mount, Semiclassical approximations in wave mechanics, *Rep. Prog. Phys.* 35 (1972) 315.
8. E. J. Heller, Frozen gaussians: a very simple semiclassical approximation, *J. Chem. Phys.* 75 (1981) 2923.
9. K. G. Kay, Semiclassical initial value treatments of atoms and molecules, *Ann. Rev. Phys. Chem.* 56 (2005) 255.
10. R. P. Feynman, Space-time approach to non-relativistic quantum mechanics, *Rev. Mod. Phys.* 20 (1948) 367.
11. R. P. Feynman, A. R. Hibbs, *Quantum mechanics and path integrals*, McGraw-Hill, New York, 1965.
12. V. S. Filinov, Calculation of Feynman integrals by means of the Monte Carlo method, *Nucl. Phys. B* 271 (1986) 717.
13. H. W. Lee, Theory and application of the quantum phase-space distribution functions, *Physics Reports* 259 (1995) 147.
14. E. Wigner, On the quantum correction for thermodynamic equilibrium, *Phys. Rev.* 40 (1932) 749.
15. V. S. Filinov, Y. V. Medvedev, V. L. Kamskyi, Quantum dynamics and Wigner representation of quantum mechanics, *Mol. Phys.* 85 (1995) 711.
16. V. S. Filinov, Wigner approach to quantum statistical mechanics and quantum generalization molecular dynamics method. part 1 & 2, *Mol. Phys.* 88 (1996) 1517 & 1529.

17. V. S. Filinov, M. Bonitz, A. Filinov, V. O. Golubnychiy, Wigner function quantum molecular dynamics, *Lecture Notes in Physics* 739 (2008) 41.
18. S. Mancini, V. I. Man'ko, P. Tombesi, Symplectic tomography as classical approach to quantum systems, *Phys. Lett. A* 213 (1996) 1.
19. S. Mancini, V. I. Man'ko, P. Tombesi, Classical-like description of quantum dynamics by means of symplectic tomography, *Found. Phys.* 27 (1997) 801.
20. V. S. Filinov, G. Schubert, P. Levashov, M. Bonitz, H. Fehske, V. E. Fortov, A. V. Filinov, Center-of-mass tomographic approach to quantum dynamics, *Phys. Lett. A* 372 (2008) 5064.
21. A. S. Arkhipov, Y. E. Lozovik, V. I. Man'ko, Center of mass tomography for reconstructing quantum states of multipartite systems, *Phys. Lett. A* 328 (2004) 419.
22. Y. E. Lozovik, V. A. Sharapov, A. S. Arkhipov, Simulation of tunneling in the quantum tomography approach, *Phys. Rev. A* 69 (2004) 022116.
23. H. Tal-Ezer, R. Kosloff, An accurate and efficient scheme for propagating the time dependent Schrödinger equation, *J. Chem. Phys.* 81 (1984) 3967–3971.
24. R. Chen, H. Guo, The Chebyshev propagator for quantum systems, *Comp. Phys. Comm.* 119 (1999) 19–31.
25. A. Weiße, H. Fehske, Chebyshev expansion techniques, *Lecture Notes in Physics* 739 (2008) 545.
26. H. F. Trotter, On the product of semi-groups of operators, *Proc. Am. Math. Soc.* 10 (1959) 545.
27. M. Suzuki, Generalized Trotter's formula and systematic approximants of exponential operators and inner derivations with applications to many-body problems, *Commun. Math. Phys.* 51 (1976) 183.
28. R. W. Hockney, J. W. Eastwood, *Computer simulation using particles*, IOP Publishing Ltd, London, 1988.
29. G. Wentzel, Eine Verallgemeinerung der Quantenbedingungen für die Zwecke der Wellenmechanik, *Z. Phys.* 38 (1926) 518.
30. H. A. Kramers, Wellenmechanik und halbzahlige Quantisierung, *Z. Phys.* 39 (1926) 828.
31. L. N. Brillouin, La mécanique ondulatoire de Schrödinger; une méthode générale de résolution par approximations successives, *Comptes Rendus (Paris)* 183 (1926) 24.
32. L. S. Schulman, *Techniques and applications of path integration*, Wiley, New York, 1981.
33. M. C. Gutzwiller, *Chaos in classical and quantum mechanics*, Springer, New York, 1990.
34. J. Milnor, *Morse theory*, Princeton University Press, Princeton, 1963.
35. M. Morse, *Variational analysis*, Wiley, New York, 1973.
36. J. H. Van Vleck, The correspondence principle in the statistical interpretation of quantum mechanics, *Proc. Nat. Acad. U. S. Sci* 14 (1928) 178.
37. M. C. Gutzwiller, Phase-integral approximation in momentum space and the bound states of an atom, *J. Math. Phys.* 8 (1967) 1979.
38. K. G. Kay, Numerical study of semiclassical initial value methods for dynamics, *J. Chem. Phys.* 100 (1994) 4432.
39. X. Sun, H. Wang, W. H. Miller, Semiclassical theory of electronically nonadiabatic dynamics: results of a linearized approximation to the initial value representation, *J. Chem. Phys.* 109 (1998) 7064.
40. H. Wang, D. E. Manolopoulos, W. H. Miller, Generalized Filinov transformation of the semiclassical initial value representation, *J. Chem. Phys.* 115 (2001) 6317.
41. M. F. Herman, E. Kluk, A semiclassical justification for the use of non-spreading

- wavepackets in dynamics calculations, *Chem. Phys.* 91 (1984) 27.
42. S. A. Deshpande, G. S. Ezra, On the derivation of the Herman-Kluk propagator, *J. Phys. A* 39 (2006) 5067.
 43. N. Makri, W. H. Miller, Monte Carlo integration with oscillatory integrands: implications for Feynman path integration in real time, *Chem. Phys. Lett.* 139 (1987) 10.
 44. A. R. Walton, D. E. Manolopoulos, A new semiclassical initial value method for Franck-Condon spectra, *Mol. Phys.* 87 (1996) 961.
 45. D. E. Dauger, V. K. Decyk, J. M. Dawson, Using semiclassical trajectories for the time-evolution of interacting quantum-mechanical systems, *J. of Comp. Phys.* 209 (2005) 559.
 46. J. Tonge, D. E. Dauger, V. K. Decyk, Two-dimensional semiclassical particle-in-cell code for simulation of quantum plasmas, *Comp. Phys. Comm.* 164 (2004) 279.
 47. C. Grosche, F. Steiner, *Handbook of Feynman path integrals*, Springer, Berlin, 1998.
 48. H. Weyl, *The theory of groups and quantum mechanics*, 2nd Edition, Dover Publications, 1950.
 49. J. E. Moyal, Quantum mechanics as a statistical theory, *Proc. Camb. phil. Soc.* 45 (1949) 99.
 50. A. S. Arkhipov, Y. E. Lozovik, New method of quantum dynamics simulation based on the quantum tomography, *Phys. Lett. A* 319 (2003) 217.
 51. S. R. Deans, *The Radon transform and some of its applications*, John Wiley & Sons, New York, 1983.
 52. A. S. Arkhipov, V. I. Man'ko, Relativistic systems and their evolution in quantum tomography, *J. Russ. Laser Res.* 25 (2004) 468.
 53. C. W. Gardiner, *Handbook of stochastic methods*, 2nd Edition, Springer, Berlin, 1990.
 54. A. A. Sveshnikov, *Applied theory of Markovian processes*, Lan, St. Petersburg, 2007.
 55. A. N. Kolmogorov, Über die analytischen Methoden in der Wahrscheinlichkeitsrechnung, *Math. Ann.* B 104 (1931) 415.
 56. W. H. Press, B. P. Flannery, S. A. Teukolsky, W. T. Vetterling, *Numerical recipes*, Cambridge University Press, Cambridge, 1986.
 57. N. Makri, Forward-backward quantum dynamics for time correlation functions, *J. Phys. C* 108 (2004) 806.
 58. X. Sun, W. H. Miller, Forward-backward initial value representation for semiclassical time correlation functions, *J. Chem. Phys.* 110 (1999) 6635.
 59. H. W. Lee, M. O. Scully, Wigner phase space description of a Morse oscillator, *J. Chem. Phys.* 77 (1982) 4604.
 60. H. W. Lee, Quantum potential in the Wigner phase space, *Phys. Lett. A* 146 (1990) 287.
 61. H. W. Lee, Wigner trajectories of a Gaussian wave packet perturbed by a weak potential, *Found. Phys.* 22 (1992) 995.
 62. G. Schubert, H. Fehske, Dynamical aspects of 2d-quantum percolation, *Phys. Rev. B* 77 (2008) 245130.
 63. H. Fehske, J. Schleede, G. Schubert, G. Wellein, A. R. Bishop, Numerical approaches to time evolution of complex quantum systems, *Phys. Lett. A* 373 (2009) 2182.